PhotoniX

RESEARCH Open Access

Ultra-wideband terahertz fingerprint enhancement sensing and inversion model supported by single-pixel reconfigurable graphene metasurface

Bingwei Liu[1], Yan Peng[1*], YuFan Hao[1], Yiming Zhu[1*], Shengjiang Chang[2*] and Songlin Zhuang[1]

*Correspondence: py@usst.edu.cn; ymzhu@usst.edu.cn; sjchang@nankai.edu.cn

[1] Terahertz Technology Innovation Research Institute, Terahertz Spectrum and Imaging Technology Cooperative Innovation Center, Shanghai Key Lab of Modern Optical System, University of Shanghai for Science and Technology, Shanghai 200093, China
[2] Institute of Modern Optics, Nankai University, Tianjin 300350, China

Abstract

The molecular fingerprint sensing technology based on metasurface has unique attraction in the biomedical field. However, in the terahertz (THz) band, existing metasurface designs based on multi-pixel or angle multiplexing usually require more analyte amount or possess a narrower tuning bandwidth. Here, we propose a novel single-pixel graphene metasurface. Based on the synchronous voltage tuning, this metasurface enables ultra-wideband (~ 1.5 THz) fingerprint enhancement sensing of trace analytes, including chiral optical isomers, with a limit of detection (LoD) ≤ 0.64 μg/mm^2. The enhancement of the fingerprint signal (~ 17.4 dB) originates from the electromagnetically induced transparency (EIT) effect excited by the metasurface, and the ideal overlap between the light field constrained by single-layer graphene (SLG) and ultra-thin analyte. Meanwhile, due to the unique nonlinear enhancement mechanism in graphene tuning, the absorption envelope distortion is inevitable. To solve this problem, a universal fingerprint spectrum inversion model is developed for the first time, and the restoration of standard fingerprints reaches $R_{max}^2 \geq 0.99$. In addition, the asynchronous voltage tuning of the metasurface provides an opportunity for realizing the dynamic reconfiguration of EIT resonance and the slow light modulation in the broadband range. This work builds a bridge for ultra-wideband THz fingerprint sensing of trace analytes, and has potential applications in active spatial light modulators, slow light devices and dynamic imaging equipments.

Keywords: Graphene metasurface, Chiral molecules, Terahertz fingerprint, Electromagnetically induced transparency, Spectrum inversion model

Introduction

THz technology has been widely applied in exploring the front-field of life science related to biological tissues, cells and even DNA scales due to its unique advantages such as nonionizing, strong penetration and excellent time resolution [1–4]. Likewise, obtaining terahertz fingerprint spectra of molecules provides a powerful tool for label-free identification of substances and in-depth study of important information such as molecular spatial structure, framework vibration, and intermolecular interaction [5–7].

In general, since the tableting samples (thickness $\geq$ mm or mass $\geq$ mg) provide sufficient light attenuation depth, conventional THz technology can easily obtain their THz absorption fingerprint features based on the Beer–Lambert law [8, 9]. However, the trace analytes (thickness $\leq$ μm or mass $\leq$ μg) collected in many scenarios have a very small absorption cross-section [10], which do not match the detection wavelength. This will lead to weak light-matter interaction and seriously hinder the application of THz technology in the field of trace analysis. Fortunately, the proposed optical metasurfaces in recent years provide the possibility to overcome this obstacle, which can confine the incident light in their resonant cavities and form a strong local near-field, thus greatly promoting the light-matter interaction [11–16]. Some reported metasurface-based THz sensing methods can obtain the refractive index frequency shift or absorption amplitude change caused by the analyte through the resonance detection peak, so as to realize the detection of samples such as cells [17–19], proteins [20–23], DNA [24, 25] and viruses [26]. However, the material and structure of previous metallic or dielectric metasurfaces are difficult to adjust after fabrication. And the isolated and narrow-band distribution characteristics of their resonance peaks will result in extremely limited information on frequency shift or amplitude change detected [27–31]. More importantly, obtaining multiple THz fingerprint features (≥ 2) of the analyte in the broadband range is the key to further study the molecular conformation and accurately distinguish different samples to avoid 'false positive' diagnosis [32–34]. Therefore, how to achieve broadband tuning and detection of resonance excited by metasurfaces has become an urgent problem to be solved.

To address this issue, resonance multiplexing methods based on multi-pixel [35] or angle manipulation [36] have been put forward. The former relies on a combination of multiple metasurfaces (10×10 Piexls) to achieve full coverage of target spectra, and the latter achieves broadband spectral tuning by manipulating the incident angle between 0° and 60°. They all realize the mid-infrared absorption fingerprint retrieval of trace analytes such as proteins through relatively discrete resonance frequencies, and similar work has been further tracked and reported [37–39]. However, considering the matching between the spot and the metasurface size in the THz band, the multi-pixel scheme usually requires fabricating and assembling a series of complex micro-nano structure arrays, and which puts forward more injection amount demands for the analyte [40]. While for the angle-multiplexed metasurface, fussy angle manipulation and deflection devices configurations are essential, and the tuning bandwidth of a single chip is relatively narrow, which will inevitably bring challenges to equipment cost and system integration [41]. Here, the convenient single-pixel metasurface design is obviously more recommended, because its chip working area can be controlled as small as possible, so as to make full use of the limited trace samples for sensing. Recently, the introduction of photoactive or electroactive materials (Germanium, Silicon, liquid–crystal and 2D materials, etc.) provides a new dimension for the tunability of resonance frequencies excited by metasurfaces, and has been used to develop optical switches [42, 43], spatial light modulation [44, 45], polarization conversion [46], beam steering [47, 48] and sensors devices [49]. Among them, graphene, as a 2D carbon atomic crystal, exhibits excellent electro-optics properties in the entire infrared region [50–52], and has good on-chip integration potential and device compatibility. And its conductivity can be continuously adjusted by

electric gating or photo-induced doping-controlled Fermi level changes. Therefore, graphene can be used as an ideal choice for the development of broadband resonance tunable metasurface [53, 54]. It is worth mentioning that the graphene resonator with only one atomic layer thickness is very conducive to the uniform coverage of trace molecules, and its bound light field can also achieve approximately perfect spatial overlap with the analyte. Those unique advantages that traditional metallic or dielectric resonators do not possess are crucial for THz fingerprint sensing of trace molecules. Because this will be more benefit for enhancing the absorption signal of the molecule, and even highlighting the weak fingerprint difference between chiral optical isomers [55].

In this work, we present a single-pixel reconfigurable graphene metasurface design based on EIT, which can realize ultra-wideband ($\sim$ 1.5 THz) THz fingerprint enhancement sensing of trace molecules and accurate identification of chiral drug optical isomers based on synchronous voltage tuning scheme, with its LoD $\leq$ 0.64 μg/mm^2. Compared with the bare substrate detection method, this metasurface provides a significant signal enhancement factor of up to 17.4 dB. To solve the problem of absorption envelope distortion caused by nonlinear enhancement mechanism in graphene tuning, a universal fingerprint spectrum inversion model is developed for the first time. And this model realizes the ideal restoration to standard fingerprint lineshapes ($R_{max}{}^2 \geq 0.99$). In addition, utilizing the naturally reconfigurable characteristics of the proposed metasurface, the asynchronous voltage tuning scheme can be executed to realize the dynamic tailoring and slow light modulation of EIT resonance in the broadband range. The coupled harmonic oscillators model is introduced to explain the related modulation mechanism. Our results show that the proposed metasurface can serve as a high-precision ultra-wideband THz fingerprint sensing platform for trace molecules and chiral optical isomers, and will be promoted and applied in the fields of active photonic sensors, optical manipulation and imaging equipments.

Design and methods

Figure 1 shows the schematic diagram of the proposed reconfigurable graphene metasurface. In the demonstrated double-channel voltage tuning scheme described in Fig. 1a, the up ring chain resonator (U-RCR) and down ring chain resonator (D-RCR) are connected with corresponding electrode contacts respectively, and the Fermi level of graphene can be manipulated by electric gating. Then, under the radiation of THz pulse, the in-plane graphene resonator with quasi-metallic properties will excite the EIT effect, and the corresponding constrained electromagnetic field will promote strong light-matter interaction. The geometric parameters of the lattice are described in Fig. 1b. Here, the periods along the x- and y-directions are $P_x = 18.5$ μm and $P_y = 37$ μm. As mentioned above, in order to facilitate the distinction, we have defined the up and down ring chain resonator in the lattice as U-RCR and D-RCR, respectively. In the x–y plane, $L = 15$ μm, $W = 2.5$ μm, $D = 3.5$ μm, $G_1 = 1.5$ μm, and $G_2 = 6$ μm. It should be noted that the adjacent periodic graphene ring chain structures are naturally connected, thus forming conductive pathways. The device architecture is shown in detail in Fig. 1c. Separate source and drain electrode combinations are distributed on the left and right sides of the top of the device. The single-layer graphene resonator arrays are configured between the electrodes, with an Al_2O_3 dielectric layer below as the isolation. The substrate material is silicon and is configured with bottom

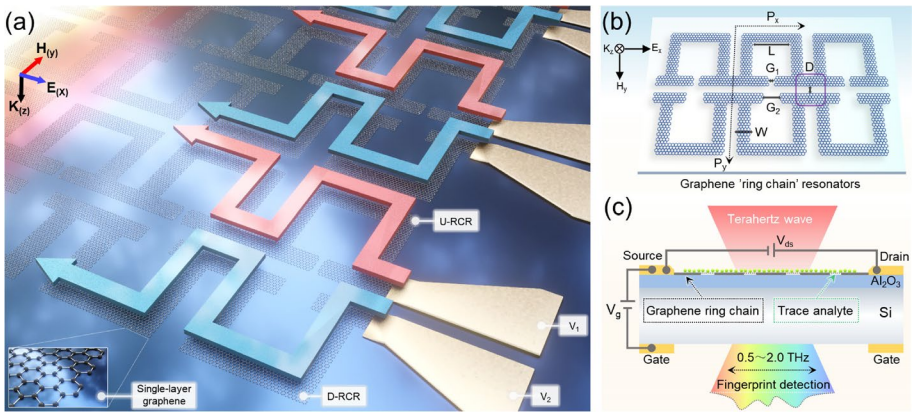

Fig. 1 Design concept of the proposed reconfigurable graphene metasurface. **a** Schematic diagram of graphene metasurface. Here, The Fermi level of graphene can be manipulated by double-channel voltage tuning, thereby achieving the multi-functional multiplexing of the metasurface in a broadband range (0.5 ~ 2.0 THz). **b** The geometric parameters of the lattice. The periods along the x- and y-directions are $P_x = 18.5$ μm and $P_y = 37$ μm. For the single-layer graphene structure in the x–y plane, L = 15 μm, W = 2.5 μm, D = 3.5 μm, $G_1 = 1.5$ μm, $G_2 = 6$ μm. The purple frame marks that adjacent periodic structures are connected as a 'ring chain'. **c** Visualization of the device architecture. The metasurface consists of top gold electrodes (source and drain electrode), single-layer graphene resonator arrays, an aluminum oxide (Al_2O_3) dielectric layer, silicon substrate, and bottom gold electrodes (gate electrode)

gate electrodes. The thicknesses of the electrodes, the dielectric layer and the silicon substrate are set to be $t_{elet} = 50$ nm, $t_{die} = 60$ nm and $t_{sub} = 300$ μm, respectively. Based on the synchronous voltage tuning scheme, THz fingerprint enhanced sensing of trace molecules in the ultra-wideband range (0.5 ~ 2.0 THz) can be realized. In addition, the asynchronous voltage tuning scheme can also be executed to achieve broadband reconstruction of EIT resonance, thereby expanding the functional application of the metasurface.

In the THz band, graphene can obtain uniform electrical doping by applying a gate voltage bias. For graphene with a single atomic layer thickness ($t_{gra} = 0.34$ nm), its electro-optics properties can be described by an effective surface conductivity model [56, 57], which includes the intraband and interband transitions:

$$\sigma_{\mathrm{gra}} = \sigma_{\mathrm{intra}} + \sigma_{\mathrm{inter}} = \frac{2e^2 k_B T}{\pi\hbar^2}\frac{i}{\omega + i/\tau}\ln\left[2\cosh\left(\frac{E_F}{2k_B T}\right)\right] + \frac{e^2}{4\hbar^2}\left[\frac{1}{2} + \frac{1}{\pi}\arctan\left(\frac{\hbar\omega - 2E_F}{2k_B T}\right) - \frac{i}{2\pi}\ln\frac{(\hbar\omega + 2E_F)^2}{(\hbar\omega - 2E_F)^2 + 4(k_B T)^2}\right] \tag{1}$$

Where e is the electron charge, k_B is the Boltzman constant, T is the operation temperature, $\hbar$ is the reduced Planck constant, ω is the angular frequency of the incident light, τ is the carrier relaxation time, and E_F is the Femi level. For the lower THz frequency domain ($\hbar\omega < 2E_F$), the contribution originated from the interband transition can be ignored according to the Pauli Exclusion Principle. Therefore, the surface conductivity of graphene can be simplified to the Drude-like model:

$$\sigma_{\mathrm{gra}} = \frac{e^2 E_F}{\pi\hbar^2}\frac{i}{(\omega + i/\tau)} \tag{2}$$

where the carrier relaxation time $\tau = (\mu E_F)/(e v_F{}^2)$, and the Fermi velocity $v_F = 1 \times 10^6$ $\mathrm{m \cdot s^{-1}}$. Here we employ carrier mobility $\mu = 2 \times 10^4$ $\mathrm{cm^2 \cdot V^{-1} \cdot s^{-1}}$, which is achievable

for the high-quality graphene obtained by the mechanical exfoliation or chemical vapor deposition (CVD) method [58–60]. In addition, the carrier relaxation time τ may have a very weak dependence on the frequency ω and the Fermi level E_F [61], but it will not significantly affect the main conclusions drawn in our work. The conductivity model predicted by the Eq. (1) and Eq. (2) shows that the electro-optics properties of graphene in the THz band can be continuously adjusted by manipulating the Fermi level. As our proposed metasurface design shows, as a classic capacitor structure, the Fermi level of graphene can be accurately manipulated by applying different gate voltages V_g according to $E_F(V_g) = \hbar v_F \sqrt{\pi a V_g}$ [62]. In addition, configuring an ultra-thin Al_2O_3 dielectric layer can effectively increase gate capacitance and improve the tuning performance of the metasurface [63]. Here, other methods, such as combining the ionic gel top grid to regulate graphene, are not preferred [64], because under the physical isolation of the gel layer, the space overlap between the confined field in graphene and the ultra-thin sample layer cannot be fully utilized in sensing.

In this work, numerical calculations were carried out using the commercial finite element software Comsol Multiphysics (version 5.6). Floquet periodic conditions were set in free space along the x- and y-directions, a perfect match layer (PML) was taken in the z-direction as the absorption boundary. The excitation field was an x- or y- polarized plane wave propagating along the z-direction. The permittivity of the Al_2O_3 dielectric layer and silicon substrate are taken as $\varepsilon_{die} = 7.5$ and $\varepsilon_{si} = 11.7$, respectively [64]. Graphene is set as a quasi-two-dimensional material characterized by transition boundary conditions (TBC). Convergence results were obtained by setting the grid smaller than the critical structure minimum size.

The fabrication process of metasurface device can follow the steps below [62, 65]: 1) An ultra-thin Al_2O_3 dielectric layer is grown on pre-doped silicon substrate by atomic layer deposition (ALD) method. 2) The prepared high-quality single-layer graphene is transferred to the top of the dielectric layer, and then uses electron beam lithography (EBL) for patterning. 3) The required gold electrode contacts are prepared by evaporation process and conventional lithography technology, and connected to the voltage sources by flying wires. In addition, some improved processes have been proposed in recent work, such as prefabricating protective layers for graphene and adding annealing steps [52, 66], which can further avoid the undesired air oxidation, photo-resist contamination and other damage to graphene, thereby improving the yield rate of devices.

Results and discussion

EIT characteristics excited by graphene metasurface

In atomic physics, the quantum in excitation states will produce a narrow transparency window with a sharp dispersive property due to the destructive interference, namely the electromagnetically induced transparency effect (EIT) [67, 68]. Inspired by this phenomenon, the EIT-like effect has been simulated in the optical waveband through the 'bright and dark' mode, the 'bright and quasi-dark' mode or the 'bright-bright' mode [69–71]. The high dispersive property of EIT effect also helps to solve the issue of radiative loss in plasmonic systems, and has unique application advantages in the sensing field [49, 72, 73].

Here the unique chain structure is employed to produce the EIT analogue. The resonance transmission spectra excited by graphene U-RCR or D-RCR alone are given in Fig. 2a, and their Fermi level are defined as E_{F1} and E_{F2}, respectively. Here, we choose the condition of $E_{F1} = E_{F2} = 2$ eV to discuss in depth. It can be found that under the x-polarized THz wave incidence, the U-RCR or D-RCR alone will excite LC resonance (LC_1 or LC_2) at 1.58 THz or 2 THz, respectively, and exhibit Lorentz lineshape. Next, in Fig. 2b, we assemble the U-RCR and D-RCR, and speculate that the EIT effect will be excited based on the coupling between the LC_1 and LC_2 resonances. And under the x-polarized incidence, a sharp transmission window (1.77 THz) with 48% efficiency appears between the two LC resonances, which validates our hypothesis. In addition, under the influence of mode coupling, the frequency position and resonance intensity of two LC resonances have also changed slightly. We also monitored the distribution and intensity histogram characteristics of the electric field in the x–y plane corresponding to three resonance features of EIT transmission spectrum. As shown in Fig. 2c, for LC_1 or LC_2 resonances, only the U-RCR or D-RCR are

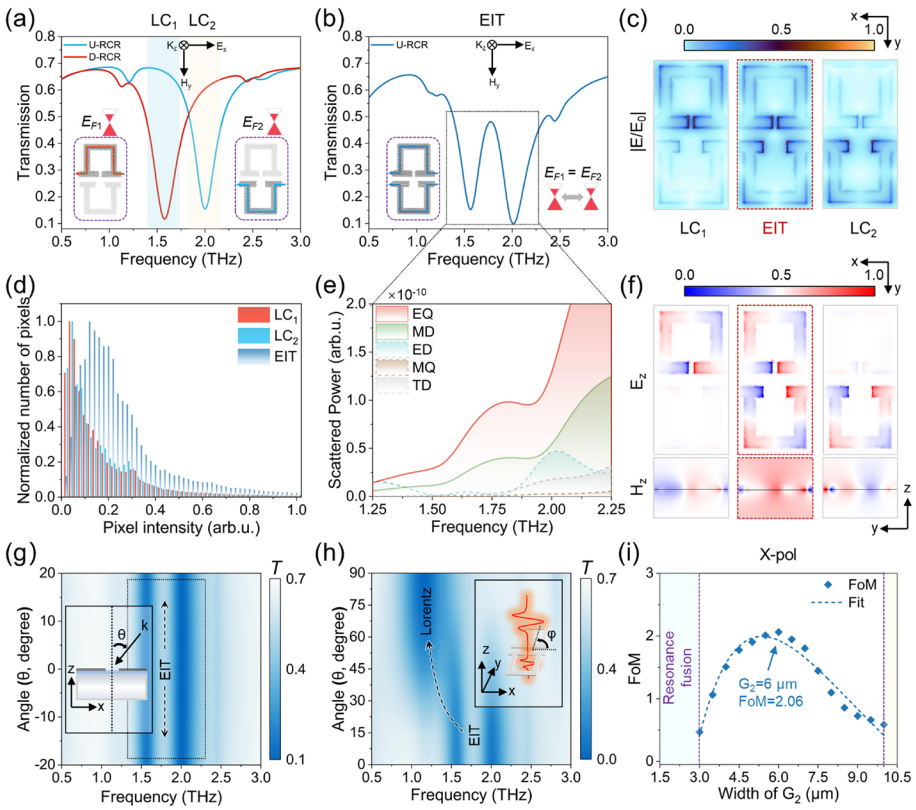

Fig. 2 The characteristics and formation mechanism of EIT resonance excited by the graphene metasurface, and the stability under various incident conditions. **a**, **b** Simulated the resonance transmission spectra (LC_1 or LC_2) excited by U-RCR or D-RCR alone, and the resonance transmission spectrum (EIT) excited by their combination, respectively. The inset gives the corresponding structures and polarization conditions. **c**, **d** The distribution and intensity histogram characteristics of the electric field in the x–y plane corresponding to the resonance positions of LC_1, LC_2, and EIT. **e**, **f** Multipolar decomposition and mode distribution of the graphene metasurface. **g**, **h** Simulated the response of graphene metasurface under non-vertical incident THz waves or different polarization angles incident THz waves. **i** Calculated the general figure of merit (FoM) values of EIT resonance corresponding different gap widths G_2. The left blue mask is the region cannot be observed due to resonance fusion. The right yellow mask is the invalid region due to the gap width larger than the structural limit. The nonlinear fit to the data points was performed, all with $R^2 > 0.99$.

excited, and current oscillations at their gap regions can be observed, which exhibit 'bright' modes. While for EIT resonance, the U-RCR and D-RCR all excite current oscillation, and overall have a wider range of strong field distribution. It can be determined that the EIT resonance are obtained by the 'bright-bright' mode coupling. In Fig. 2d, the intensity histogram characteristics of above electric field distributions are statistically analyzed. The gray levels corresponding to the background fields of LC_1 or LC_2 resonance occupy most of the pixels. But for EIT resonance, the gray level corresponding to its background field occupies less pixel values, and that of the working light field occupies more pixel values with relatively uniform distribution in general. The area integrals of the intensity distribution histogram corresponding to LC_1, LC_2 and EIT resonance are calculated, and the result ratio is $AS_{LC_1} : AS_{LC_2} : AS_{EIT} = 7 : 6.5 : 14$. Obviously, the mode distribution of EIT resonance is more beneficial for sensing applications, because the trace sample attached to the sensor may exhibit an uneven distribution in actual detection. And the larger 'hot spot area' will promote sensor to capture more sample molecules, thereby improving the efficiency of light-matter interaction.

In order to further analyze the physical mechanism of the excited EIT effect, we performed the Cartesian multipolar decomposition for the far-field scattering power of graphene metasurface, which mainly includes electric dipole (ED), magnetic dipole (MD), electric quadrupole (EQ), magnetic quadrupole (MQ) and toroidal dipole (TD). Here, the high-order components of multipole expansion are ignored in calculation because their contributions are very small (see Supplementary Material Section 1 for details). As shown in Fig. 2e, the EIT resonance is mainly controlled by EQ, and the contribution of MD cannot be ignored, with other multipolar components are being strongly inhibited. Correspondingly, the surface current distribution in the x–y plane and the z component of the magnetic field in the y–z plane corresponding to the EIT and two adjacent LC resonance positions are supplemented in Fig. 2f. It can be found that for the EIT resonance, both the U-RCR and D-RCR excite the radiative EQ mode and have an overall strong magnetic field distribution (Fig. 2f, middle). While for the two adjacent LC resonances, only the EQ mode and magnetic field distribution corresponding to the position of the U-RCR or D-RCR are excited (Fig. 2f, left and right). In addition, the response of graphene metasurface under non-vertical incident THz waves are considered in Fig. 2g. Under the x-polarization condition, the metasurface maintains nearly 100% linear stability for the non-vertical incidence angle within $\pm 20°$. Figure 2h also shows the response of graphene metasurface under different polarization angles incident THz waves. It can be found that the metasurface exhibits good polarization-insensitivity in the range of 0° to 30°. Interestingly, the switching from EIT resonance to Lorentz resonance is observed in the range of 30° to 90°. We believe that this phenomenon may have potential important applications and plan to discuss it specifically in future work. It should be noted that the cavity gap widths ($G_1 = 1.5$ μm, $G_2 = 6$ μm) used in the U-RCR or D-RCR is the result of optimization. Here, G_1 is fixed at 1.5 μm and adjust the size of G_2. A general figure of merit (FoM) [42] is introduced to obtain the best tradeoff between Q factor and resonance intensity, and it obeys $\mathrm{FoM} = \mathrm{Q} \times \mathrm{I}$, where Q and I are the quality factor and resonance intensity of EIT peak, respectively. In Fig. 2i, for the metasurface at $G_2 = 6$ μm, the EIT resonance excited under x-polarization condition corresponds to $\mathrm{FoM}_{\max} = 2.06$. Different from the traditional refractive index frequency shift sensing scheme, we focus

on the detection of trace molecular broadband absorption fingerprints. Therefore, the robustness and strong resonance intensity of EIT peak are particularly important. We consider that structural parameters ($G_1 = 1.5$ μm, $G_2 = 6$ μm) are the ideal results obtained by optimization, and this scheme is used for analysis in the following work.

Broadband tuning and sensing performance of EIT resonance

Based on the above studies of the EIT resonance mechanism, we next investigate its broadband tuning and sensing performance under the synchronous voltage tuning scheme. As shown in Fig. 3a, the synchronous voltages ($V_1 = V_2$) are applied to the U-RCR and D-RCR, so that their Fermi levels can be manipulated to change consistently. Under the incidence of x-polarized THz waves, since the LC_1 and LC_2 resonances satisfies the coupling condition, the generated EIT resonance can be freely tuned in a broadband range with the increase of Fermi levels. The broadband tuning spectra and scanning envelope of EIT resonance are given in Fig. 3b and c. When the Fermi levels ($E_{F1} = E_{F2}$) changes from 0.1 eV to 2.5 eV, the peak frequency of EIT drifts from 0.5 THz to 2 THz, thus achieving continuous tuning in the ultra-wideband range of ~ 1.5 THz. It is worth noting that the EIT peak exhibits nearly horizontal displacement characteristics within this bandwidth range. And its sweeping envelope is intuitive and has robustness, which is helpful for the post-processing of trace molecular sensing fingerprint data. The sweeping resolution of the EIT resonance can also be freely adjusted, which depends on the performance of the matched voltage source system. In addition,

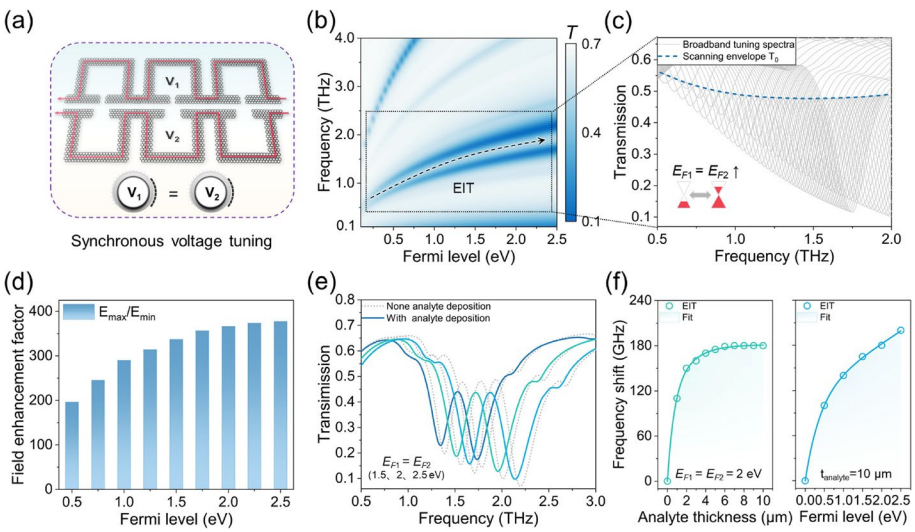

Fig. 3 The broadband tuning and sensing performance of EIT resonance under the synchronous voltage tuning scheme. **a** Applied synchronous bias voltages ($V_1 = V_2$) to the U-RCR and D-RCR for manipulating the Fermi level. **b**, **c** The broadband tuning transmission spectra of EIT resonance. The black frame marks the scanning range of EIT resonance (0.5 ~ 2.0 THz). The cyan dotted line marks the sweeping envelope of EIT resonance. **d** Extracted the local electric field enhancement factors corresponding to the EIT resonance at different Fermi levels. **e** The perturbation effect of the ultra-thin sample layer ($\tilde{n} = 1.5 + 0.2i$) with a thickness of 1 μm, and here the EIT resonance corresponds to $E_{F1} = E_{F2} = 1.5, 2, 2.5$ eV. **f** The refractive index frequency shift caused by analytes with different thickness, and here the EIT resonance corresponds to $E_{F1} = E_{F2} = 2$ eV (left panel). The maximum refractive index frequency shift caused by analyte with a thickness of 10 μm, and here the EIT resonance corresponds to different Fermi levels (right panel). And the refractive index of analytes is 2 RIU

as the Fermi level increases, the resonance intensity of EIT peak becomes stronger and maintains a large amplitude of 10% ~ 50% in the range of > 1 THz. Therefore, facing the problem of lineshape decay caused by sample absorption during testing, this metasurface can ensure stable EIT sensing and recognition capabilities, and has high suitability to commercial THz spectrometers.

In Fig. 3d, it can be found that the electric field enhancement factors of EIT resonance at 0.5 eV and 2.5 eV are 196 and 377, respectively. Considering that this difference is far less than one order of magnitude, we speculate that the sensing performance of EIT resonance has consistency in the broadband range. As shown in Fig. 3e, a layer of ultra-thin analyte with a thickness of 1 μm is simulated and deposited on the metasurface. Considering the subsequent samples to be tested, we define its complex refractive index as $\widetilde{n} = 1.5 + 0.2i$. It can be found that the very obvious lineshape perturbation responses are observed at EIT resonances corresponding to $E_{F1} = E_{F2} = 1.5$, 2, 2.5 eV. And the relative changes of EIT peak amplitude are very approximate, which is beneficial for detecting broadband fingerprints of trace molecules. In addition, for THz fingerprint retrieval, the contribution of refractive index frequency shift sensing is almost negligible. But for completeness, we show the refractive index sensing performance of graphene metasurface in Fig. 3f. Here, the refractive index of the thin-layer analyte is set to 2 RIU, where RIU is the refractive index unit. And the frequency shift caused by analyte is calculated as $\Delta f = f(t) - f(t_0)$, where $f(t)$ is the resonant frequency when the analyte thickness is t μm, and $f(t_0)$ is the resonant frequency when the analyte thickness is 0 μm (bare metasurface). Taking the EIT resonance corresponds to $E_{F1} = E_{F2} = 2$ eV as an example, the Δf increases with the growth the of analyte thickness (1 ~ 10 μm) and reaches saturation at 10 μm (Fig. 3f, left). This phenomenon can be attributed to the fringing field effect of graphene metasurface when constraining the electromagnetic energy [56]. It is worth noting that for the ultra-thin analyte of 1 μm, the Δf response of EIT resonance is 117 GHz, and accounts for 65% of the maximum Δf (180 GHz), which means the metasurface is more sensitive to thin-layer analyte. In other words, it shows that most of the light field energy is confined to the near-surface of the graphene resonator. Therefore, making full use of the spatial overlap between the electromagnetic field constrained by single-layer graphene and the ultra-thin sample (≤ 1 μm) will be more beneficial for enhancing and obtaining the weak absorption fingerprint signal of trace molecules. At the same time, as the Fermi level increases, the maximum Δf corresponding to EIT resonance also increases, that is because the quasi-metallic properties of graphene is also synchronously enhanced (Fig. 3f, right). Here we introduce $S = \Delta f / \Delta n$ to describe the refractive index sensitivity of the metasurface, where Δn is the unit change of the analyte refractive index, and the maximum sensitivity is calculated as $S_{max} = 220$ GHz/RIU.

Ultra-wideband fingerprint detection and optical isomers identification of trace chiral carnitine molecules

After the discuss of broadband tuning and sensing mechanism of graphene metasurface, we further evaluate its fingerprint retrieval performance for trace molecules. The carnitine molecule ($C_7H_{15}NO_3$) is selected as the analyte to be tested, and its chiral optical isomers were L-carnitine and D-carnitine, respectively. It is of great significance to realize fingerprint identification of chiral carnitine molecules due to their

different pharmacological effect and nutritional value [55]. The standard complex refractive indexes of L-carnitine and D-carnitine in the THz band are given in Fig. 4a and d, respectively. It can be noted that the real parts of their refractive indexes are almost the same, which are difficult to be identified by the refractive index frequency shift sensing method. And they all have two absorption feature peaks with the same frequency position (1.39 THz and 1.72 THz), and the peak amplitude differences are very small. Obviously, for trace chiral carnitine samples (thickness $\leq$ μm or mass $\leq$ μg), it is a great challenge to obtain their absorption fingerprint spectra and realize the identification of chiral optical isomers. Here, an ultra-thin molecular coating with a thickness of 1 μm is simulated and deposited on graphene metasurface (Fig. 4b and e, insets). Meanwhile, the single-pixel metasurface sensing method is adopted, which is only based on one kind of resonantor unit to form the periodic array, and relies on a single chip to complete the broadband fingerprint detection of trace samples. Under the synchronous voltage tuning scheme, the fingerprint retrieval and signal

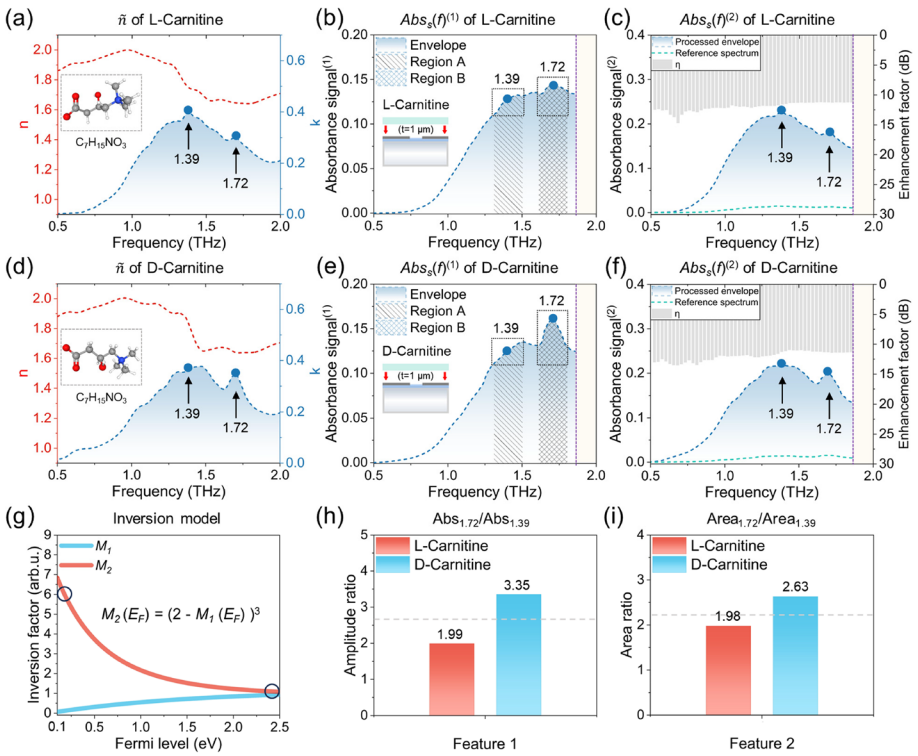

Fig. 4 Ultra-wideband THz fingerprint retrieval and identification of chiral molecules under the synchronous voltage tuning scheme. An ultra-thin molecular coating with a thickness of 1 μm is introduced for analysis. **a**, **d** The complex refractive index of chiral drug molecules L-carnitine and D-carnitine. The insets give their molecular formulas and chiral structural features. **b**, **e** The first-order absorption fingerprint envelopes of trace L-carnitine and D-carnitine molecules obtained by broadband retrieval based on graphene metasurface. The inset shows the molecular coatings deposited on the metasurface. The yellow mask is the non-applicable (N/A) area. The black frame marks the calculation range of the areas under the peaks to be obtained. **c**, **f** The second-order absorption fingerprint envelopes, the natural absorption spectra and the calculated signal enhancement factors of trace L-carnitine and D-carnitine molecules. **g** The developed nonlinear fingerprint spectral inversion model. **h**, **i** Extracted the ratios of absorption peak amplitudes and the ratios of areas under the absorption peak in the first-order absorption fingerprint envelopes corresponding to trace L-carnitine and D-carnitine molecules

processing of the samples were performed in the broadband range by EIT resonance, so as to accurately obtained the molecular fingerprint spectra of L-carnitine and D-carnitine in the range of 0.5 ∼ 2.0 THz. In this process, we first define the fingerprint signal retrieved directly by the metasurface as the first-order absorption fingerprint envelope $Abs_s(f)^{(1)}$. Secondly, we perform signal processing on $Abs_s(f)^{(1)}$, and the result is defined as the second-order absorption fingerprint envelope $Abs_s(f)^{(2)}$. The first-order absorption fingerprint envelopes of L-carnitine and D-carnitine are shown in Fig. 4b and e, which are determined by the following equation:

$$Abs_s(f)^{(1)} = 1 - \frac{T_s(f)}{T_0(f)} \tag{3}$$

Where $T_s(f)$ is the EIT peak amplitude after introducing the analyte, and $T_0(f)$ is the original EIT peak amplitude. Due to the nonlinear optical field enhancement mechanism of graphene in the Fermi level tuning, the $Abs_s(f)^{(1)}$ of L-carnitine or D-carnitine exhibits a certain distortion compared with the standard fingerprint lineshape. But they still maintain a unique corresponding relationship with their respective standard fingerprint spectra. More excitingly, the weak difference in the absorption feature peaks of L-carnitine and D-carnitine at the relative high frequency position (1.72 THz) is significantly enhanced, so that they can be directly distinguished. That can be attributed to the proposed metasurface improves the efficiency of light-matter interaction through several mechanisms, including the larger 'hot spot area' provided by EIT effect and the ideal overlap between the ideal overlap between the light field constrained by single-layer graphene and ultra-thin analyte.

To deal with the absorption envelope distortion caused by graphene tuning, a universal fingerprint spectrum inversion model is developed for the first time (Fig. 4g). And it can convert the $Abs_s(f)^{(1)}$ signal of the analyte into the $Abs_s(f)^{(2)}$ signal, thereby realizing the restoration to standard fingerprints:

$$M_2(E_F) = (2 - M_1(E_F))^n (E_F \in [0.1, 2.5], n \geq 3) \tag{4}$$

Where $M_1(E_F)$ is obtained by fitting the local electric field enhancement factors corresponding to the EIT resonance at different Fermi levels and its normalization (see Supplementary Material Section 2 for details), and n is the correction index, here take 3. It should be noted that there is a one-to-one mapping relationship between the interval of independent variate E_F and the range of its corresponding EIT peak frequency positions (see Supplementary Material Section 3 for details). Therefore, the $Abs_s(f)^{(2)}$ signals of analytes can be obtained by $Abs_s(f)^{(1)} * M_2$.

Figure 4c and f show the $Abs_s(f)^{(2)}$ signals (cyan dotted lines) of L-carnitine and D-carnitine obtained by the fingerprint spectrum inversion model, and their envelope profiles are basically consistent with their respective standard fingerprint lineshapes. The correlation coefficient R^2 is introduced to quantitatively evaluate their similarity. For L-carnitine and D-carnitine, their similarities are $R^2 \geq 0.99$ and $R^2 \geq 0.98$ (see Supplementary Material Section 4 for details), respectively. Compared with the natural absorption spectra (green dotted lines) of L-carnitine and D-carnitine obtained on the bare substrate, the final fingerprint signals ($Abs_s(f)^{(2)}$) have been greatly

enhanced in the ultra-wideband range of ~ 1.5 THz. Here, the frequency-dependent signal enhancement factor η is defined to describe the fingerprint enhancement performance of graphene metasurface [38]:

$$\eta = 10\lg\left[\frac{\int_{f_2}^{f_1} Abs_s(f)^{(2)} df}{\int_{f_2}^{f_1} Abs_r(f) df}\right] \tag{5}$$

Where $Abs_s(f)^{(2)}$ and $Abs_r(f)$ are the second-order absorption fingerprint envelope and the natural absorption spectrum, respectively. f_1 and f_2 represent the starting and ending points of the frequency interval, respectively. We calculated the broadband signal enhancement factors of trace L-carnitine and D-carnitine analytes (Fig. 4c and f, top). Their overall distribution is relatively consistent, and the maximum enhancement factors obtained are 14.7 dB and 13.5 dB, respectively. Therefore, the proposed metasurface demonstrates its broadband fingerprint sensing ability for ultra-thin chiral carnitine molecular coating with a thickness of 1 μm, and which corresponds to the LoD ≤ 0.64 μg/mm^2. For commercial THz spectrometers, their signal-to-noise ratio (SNR) can be greater than 60 dB, so the LoD of the proposed metasurface has the potential to improve by at least one order of magnitude in theory.

In the previous discussion, the first-order absorption fingerprint envelope $Abs_s(f)^{(1)}$ signals obtained by metasurface retrieval has intuitively highlighted the absorption difference of trace carnitine chiral molecules, so that their optical isomers can be qualitatively distinguished directly. Furthermore, we proposed a quantitative identification method of carnitine chiral molecules based on the ratios of absorption peak amplitudes and the ratios of areas under the absorption peak. In Fig. 4b and e, we also selected the absorption feature peaks of L-carnitine and D-carnitine and calculated their areas under the peaks in black frames, respectively. Here, the area under the peak of the feature peak at 1.39 THz ranges from 1.30 THz to 1.50 THz and that of the feature peak at 1.72 THz ranges from 1.61 THz to 1.81 THz. The ratios of absorption peak amplitudes and the ratios of areas under the absorption peak corresponding to L-carnitine and D-carnitine are given in Fig. 4h and i. It can be found that the feature parameters of L-carnitine (1.99, 1.98) are smaller than those of D-carnitine (3.35, 2.63), thus realizing the quantitative identification of them. More importantly, this definite intrinsic ratio relationship will not be affected by the change of sample content and has great robustness. And this quantitative method is expected to be popularized and applied in the fingerprint identification of other chiral samples in the future.

Ultra-wideband fingerprint detection of trace disease marker GABA molecule

To demonstrate the broad-spectrum performance of proposed metasurface in broadband fingerprint retrieval, and to verify the universality of developed fingerprint spectrum inversion model, the γ-aminobutyric acid (GABA, $C_4H_9NO_2$) is also selected as the analyte to be tested. As a neurotransmitter in brain nerve cells, GABA is the key biomarker molecule to characterize the symptoms of glioma disease. And it is difficult to realize the fingerprint detection of trace GABA molecules in clinical diagnosis [74, 75]. The standard complex refractive index of GABA in the THz band is given in Fig. 5a. It can be found that GABA has two obvious absorption feature peaks

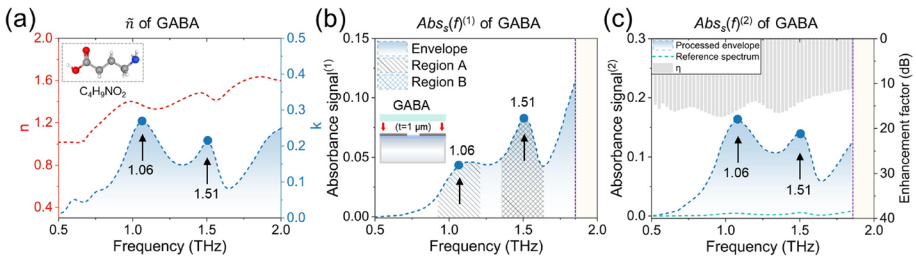

Fig. 5 Ultra-wideband THz fingerprint retrieval of trace disease marker GABA molecule under the synchronous voltage tuning scheme. An ultra-thin molecular coating with a thickness of 1 μm is introduced for analysis. **a** The complex refractive index of GABA molecule. The inset gives its molecular formula and structural features. **b** The first-order absorption fingerprint envelope of trace GABA molecule obtained by broadband retrieval based on graphene metasurface. The inset shows the molecular coatings deposited on the metasurface. The yellow mask is the non-applicable (N/A) area. **c** The second-order absorption fingerprint envelope, the natural absorption spectrum and the calculated signal enhancement factors of trace GABA molecule

(1.06 THz and 1.51 THz). Here, an ultra-thin molecular coating with a thickness of 1 μm is simulated and deposited on the metasurface, and the single-pixel metasurface sensing method is still adopted. And under the synchronous voltage tuning scheme, the molecular fingerprint spectra of GABA in the ultra-wideband range of 0.5 ~ 2.0 THz were accurately obtained. As shown in Fig. 5b, the first-order absorption fingerprint envelope $Abs_s(f)^{(1)}$ of GABA is uniquely corresponding to its standard fingerprint spectrum, and can be directly distinguished from the chiral carnitine molecules or other samples due to their different fingerprint characteristics. Figure 5c gives the second-order absorption fingerprint envelope $Abs_s(f)^{(2)}$ of GABA (cyan dotted line) processed according to the developed fingerprint spectrum inversion model, and its envelope profile is very consistent with the standard fingerprint lineshape. For GABA, the calculated similarity between its $Abs_s(f)^{(2)}$ signal and its standard fingerprint lineshape is $R^2 \geq 0.96$ (see Supplementary Material S4 for details). This result further proves the universality of our proposed fingerprint spectrum inversion model. And in the future, this model is expected to provide important inspiration and reference for the signal processing in fingerprint sensing based on graphene metasurfaces. In addition, compared with the natural absorption spectrum (green dotted lines) of GABA obtained on the bare substrate, the final fingerprint signals $Abs_s(f)^{(2)}$ have also been greatly enhanced in the ultra-wideband range of ~ 1.5 THz. The corresponding broadband enhancement factor has a relatively consistent overall distribution, and the maximum enhancement factor obtained is 17.4 dB. Therefore, the proposed metasurface demonstrates its broadband fingerprint sensing ability for ultra-thin GABA molecular coating with a thickness of 1 μm, and which corresponds to the LoD ≤ 1.11 μg/mm^2.

To indicate the superiority of our single-pixel graphene metasurface sensing scheme in detecting trace molecular fingerprints, we compared its performance with the recently reported works in Table 1. For the classic multi-pixel fingerprint sensing scheme, it often represents the combination of a series of chips, which are integrated by multi-block periodic arrays consisted of different types of resonantor units. This type of design inevitably requires the fabrication and assembly of a series of complex micro-nano structure arrays, and usually have relatively discrete resonance frequencies and low spectral resolution. In the THz band, such schemes may increase the corresponding fabricating and

Table 1 Broadband fingerprint sensing performance of recently reported metasurfaces

Material of metasurface	Resonance type	Multiplexed scheme	Spectral range	Tuning bandwidth	Analyte	Enhancement Factor	Ref
Ge	QBIC resonance	Single-pixel Angle-multiplexed	Mid-IR	~700 nm	PMMA	16.9 dB	[36]
Silicon	Mie resonance	Single-pixel Angle-multiplexed	Mid-IR	~1005 nm	2, 4-DNT	10 dB	[39]
Silicon	Mie resonance	Multi-pixel Geometry-multiplexed	Mid-IR	~400 nm	Protein A/G	17.7 dB	[35]
graphene	Plasma resonance	N/A Voltage tuning	Mid-IR	~550 nm	Protein A/G	N/A	[53]
SiO_2	QBIC resonance	N/A Thickness-multiplexed	THz	~0.8 THz	Histidine	25 dB	[76]
PE	Guided-mode resonance	N/A Angle-multiplexed	THz	~0.5 THz	α-lactose	10 dB	[41]
Graphene + Au	Diopole resonance	Multi-pixel Voltage tuning	THz	~1 THz	Glucose	6 dB	[40]
Graphene	EIT resonance	Single-pixel Voltage tuning	THz	~1.5 THz	Chiral carnitine	17.4 dB	**This work**

on-chip integration costs, and puts forward more injection amount demands for the analyte. While for the angle-multiplexed metasurface design, a single chip usually has a narrow tuning bandwidth in the THz band, and fussy angle manipulations and deflection devices configurations are essential [77, 78]. We also note that the reference [76] provides a microfluidic-based thickness-multiplexed fingerprint sensing metasurface design. By adjusting the pumping amount of the trans-decalin filler in the microfluidic channel composed of SiO_2 and Topas, thus changing thickness of the substrate, and theoretically obtaining a frequency tuning range of ~ 0.8 THz. However, this design requires the introduction of an additional microelectromechanical operating system, which may limit the modulation speed of the substrate thickness and bring challenges to the miniaturization and integration of the system. In addition, for the trace samples collected in the actual detection, it is crucial to achieve sufficient matching between sample content and chip sensing region. The recently reported works may cause the redispersion of trace samples collected, or the problem that chip sensing region cannot be completely coated. And the recollection of trace samples for reuse will bring additional operating steps and the problem of sample secondary loss. While for our single-pixel metasurface sensing scheme, it will use a smaller chip area to match more samples, thereby optimizing the detection conditions for trace samples. Obviously, compared with the works reported in the above references, our proposed single-pixel graphene metasurface design has irreplaceable advantages in comprehensive comparison including chiral molecular fingerprint enhancement, tuning bandwidth, resonance modulation convenience, system simplification and on-chip integration.

Reconfigurable characteristics of EIT resonance and its application

In this work, our proposed graphene metasurface also deliver natural reconfigurable characteristics. For example, the dynamic tailoring, reconstruction and slow light modulation of EIT resonance in the ultra-wideband range can be easily achieved under the asynchronous voltage tuning scheme. The specific scheme is shown in Fig. 6a. In the initial condition, the voltage of U-RCR and D-RCR is consistent ($V_1 = V_2$). Then, keep V_1 unchanged and change V_2 continuously. This series of voltage tuning can manipulate the Fermi level E_{F2} corresponding to D-RCR, thus changing electro-optics properties of graphene, and which can realize the active modulation of EIT effect. Figure 6b shows the evolution process of EIT resonance lineshape corresponding to initial tuning condition of $E_{F1} = E_{F2} = 2$ eV. It can be found that when E_{F1}= 2 eV remains unchanged, as E_{F2} changes from 2 eV to 1.1 eV, the EIT lineshape gradually decays and eventually switches to Lorentz lineshape, thus achieving an ideal modulation depth of 100%. It is well known that the EIT phenomenon is always accompanied by extreme modification in dispersion characteristics, which leads to the generation of slow light effect. Here, the slow light effect can be described by the group delay t_g [79]:

$$t_g = -\frac{d\varphi}{d\omega} \tag{6}$$

Where φ is the transmission phase shift and $\omega = 2\pi f$ is the angular frequency. We calculated the group delay response during the entire modulation process of EIT resonance (Fig. 6c), and extracted its peak group delay attenuation curve (Fig. 6d). It can

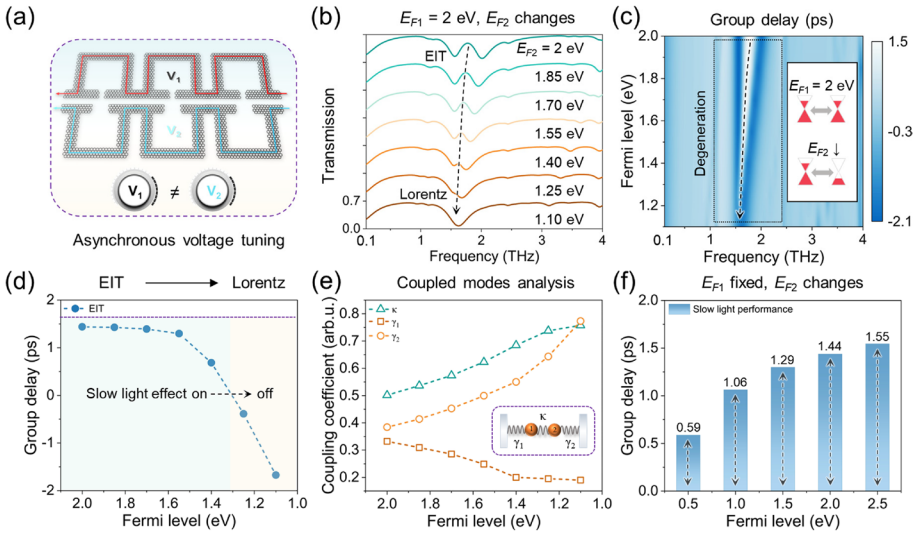

Fig. 6 The dynamic tailoring, reconstruction and slow light modulation of EIT resonance under the asynchronous voltage tuning scheme. **a** Applied asynchronous bias voltages ($V_1 \neq V_2$) to the U-RCR and D-RCR for manipulating the Fermi level. **b** The evolution process of EIT resonance lineshape excited by graphene metasurface. The Fermi level E_{F1} of U-RCR is fixed at 2 eV, and the Fermi level E_{F2} of D-RCR is manipulated to change from 2 eV to 1.1 eV. **c**, **d** The evolution process of group delay corresponding to EIT resonance, and the peak group delay attenuation curve. **e** The dependence of γ_1, γ_2, and κ extracted by fitting the EIT resonance lineshape according to the coupled harmonic oscillators model. The inset gives the simplified schematic diagram of this model. **f** The tunable slow light performance achieved by manipulating E_{F2} in the broadband range under the freely configured asynchronous voltage tuning scheme. Here E_{F1} and E_{F2} all correspond to the same initial tuning conditions

be found that in the process of switching from EIT lineshape to Lorentz lineshape, the peak group delay shows a decreasing trend until the metasurface completely loses its slow light capability.

Here, the coupled harmonic oscillators model [80] is introduced to analyze the intrinsic physical mechanism of this modulation process. In this model, the harmonic oscillator 1 and the harmonic oscillator 2 represent the U-RCR and D-RCR structures in the metasurface unit, respectively. They are driven by the incident electric field $E = E_0 e^{iwt}$ and can be described as:

$$\ddot{\chi}_1(t) + \gamma_1 \dot{\chi}_1(t) + {\omega_{01}}^2 \chi_1(t) + \kappa^2 \chi_2(t) = g_1 \frac{E_0}{m_1} \tag{7}$$

$$\ddot{\chi}_2(t) + \gamma_2 \dot{\chi}_2(t) + {\omega_{02}}^2 \chi_2(t) + \kappa^2 \chi_1(t) = g_2 \frac{E_0}{m_1} \tag{8}$$

Where χ_1, χ_2, γ_1, γ_2 represent the amplitudes and damping rates of two harmonic oscillators. ω_{01} and ω_{02} represent the resonance frequencies of two harmonic oscillators, respectively. m_1 and m_1 represent the effective masses of two harmonic oscillators. g_1 and g_2 represent the coupling strength coefficients between the two harmonic oscillators and the incident electric field $E = E_0 e^{iwt}$. κ is the coupling strength between two harmonic oscillators. By solving the Eq. (7) and Eq. (8), the susceptibility χ of graphene metasurface can be obtained as follows:

$$\chi_{eff} = \chi_{eff\_r} + i\chi_{eff\_i} = \frac{P}{\varepsilon_0} = \frac{K}{A^2B}\left[\frac{A(B+1)\kappa^2+A^2\left(\omega^2-{\omega_{02}}^2\right)+B\left(\omega^2-{\omega_{01}}^2\right)}{\kappa^4-\left(\omega^2-{\omega_{01}}^2+i\omega\gamma_1\right)\left(\omega^2-{\omega_{02}}^2+i\omega\gamma_2\right)}\right. \\ \left. +i\omega\frac{A^2\gamma_2+B\gamma_1}{\kappa^4-\left(\omega^2-{\omega_{01}}^2+i\omega\gamma_1\right)\left(\omega^2-{\omega_{02}}^2+i\omega\gamma_2\right)}\right] \tag{9}$$

Where χ_{eff_r} and χ_{eff_i} represent the dispersion and absorption in graphene metasurface, respectively. K is the proportionality factor, and $A = g_1/g_2$, $B = m_1/m_2$. Since the imaginary part of susceptibility χ is proportional to the energy dissipation, so the transmission T can be described as:

$$T = 1 - \mathrm{Im}\left(\chi_{eff}\right) \tag{10}$$

Based on this theory, we analyzed the coupling modes of EIT transmission spectra corresponding to different E_{F2} in Fig. 6b, and whose results is given in Fig. 6e. It can be found that as the Fermi level E_{F2} changes from 2 eV to 1.1 eV, the quasi-metallic properties of graphene D-RCR decays obviously, and the damping rate γ_2 corresponding to harmonic oscillator 2 increases significantly. This means that the radiation loss further increases, thereby reducing the efficiency of the transmission window, which is the main reason for the dynamic modulation of EIT resonance and its slow light effect. At the same time, the damping rate γ_1 of harmonic oscillator 1 decreases slightly, and the resonance intensity of the corresponding Lorentz lineshape is also slightly enhanced. It is worth noting that the coupling strength κ becomes larger, which may benefit from the resonance degeneracy phenomenon when the harmonic oscillator 1 and 2 are close to each other.

In Fig. 6f, we also provide examples of the peak group delay corresponding to different initial tuning conditions of E_{F1} and E_{F2}. Under the scheme of fixing E_{F1} and changing E_{F2}, the graphene metasurface can realize dynamic modulation in different slow light intervals. And the electro-optics properties of graphene determined by different E_F only lead to differences in slow light performance and do not affect the application of this metasurface as a slow light switch. In addition, for the asynchronous voltage tuning scheme adopted, it has the advantage of flexible configuration. On the one hand, the voltage of U- or D-RCR in the unit can be randomly selected to be fixed and then change the voltage of the other RCR. On the other hand, the initial tuning condition of $E_{F1} = E_{F2}$ can be freely manipulated, and then the EIT resonance can be modulated from different frequency positions (see Supplementary Material Section 5 for details). Accordingly, we can accurately realize the dynamic tailoring, reconstruction and slow light effect modulation of EIT resonance at any frequency point in the ultra-wideband range ($\sim$ 1.5 THz). In the latest reported work, voltage modulation speed of graphene up to the GHz level has been achieved based on the function generator, and it is highly feasible to transfer this technology to our synchronous or asynchronous tuning scheme [81]. At the same time, the EIT effect simulated in the metasurface has been applied in developing advanced slow light and nonlinear enhancement devices [82, 83], and achieving active modulation and ideal group delay control of EIT in the THz band have great application prospects in the future 6G and optical communication networks [84, 85]. We believe that the proposed graphene metasurface can not only serve as a high-performance active photonic sensor, but also can be well extended to many fields, such as developing spatial light modulators, ultra-high-speed terahertz communications and dynamic imaging devices.

Conclusion

In summary, we have demonstrated a new EIT-based reconfigurable graphene metasurface design and its applications. Based on synchronous voltage tuning scheme, this metasurface can realize single-pixel fingerprint retrieval of trace molecules in the broadband range ($\sim$ 1.5 THz) and the identification of optical isomers of chiral drugs, with its LoD $\leq$ 0.64 μg/mm^2. And the larger 'hot spot area' provided by EIT effect and the ideal overlap between the ideal overlap between the light field constrained by single-layer graphene and ultra-thin analyte provide an opportunity to achieve the significant enhancement of fingerprint signal ($\sim$ 17.4 dB). A universal fingerprint spectrum inversion model is proposed for the first time, which effectively solves the inherent envelope signal distortion of graphene metasurface in fingerprint retrieval. And this model realizes the ideal restoration to standard fingerprint lineshapes ($R_{max}^2 \geq 0.99$). In addition, the multi-functional multiplexing of this metasurface is also realized by executing asynchronous voltage tuning scheme, including dynamic reconstruction of EIT resonance and slow light modulation. Significantly, these function applications have tunability in the broadband range and are expected to achieve GHz-level modulation speed. Our work provides an ideal platform to realize ultra-wideband THz fingerprint sensing of various trace molecules, and have potential application scenarios in the fields of spatial light modulators, optical communication networks, and high-speed THz imaging.

Abbreviations

THz	Terahertz
EIT	Electromagnetically induced transparency
SLG	Single-layer graphene
U-RCR	Up ring chain resonator
D-RCR	Down ring chain resonator
PML	Perfect match layer
TBC	Transition boundary condition
ALD	Atomic layer deposition
EBL	Electron beam lithography
ED	Electric dipole
MD	Magnetic dipole
EQ	Electric quadrupole
MQ	Magnetic quadrupole
TD	Toroidal dipole

Supplementary Information

The online version contains supplementary material available at https://doi.org/10.1186/s43074-024-00129-4.

Additional file 1: Section 1. The Cartesian multipolar decomposition. **Section 2.** The local electric field enhancement factors corresponding to the EIT resonance at different Fermi levels and the fitting curve. **Section 3.** The mapping relationship between EIT resonance frequencies and the Fermi levels. **Section 4.** The similarity calculation of spectra obtained based on the fingerprint spectrum inversion model processing. **Section 5.** The dynamic tailoring, reconstruction and slow light modulation of EIT resonance at different frequency positions in the broadband range.

Authors' contributions

Bingwei Liu: Investigation, Methodology, Software, Data analysis, Writing – original draft and editing. Yan Peng: Funding acquisition, Supervision, Writing – Review and editing. YuFan Hao: Investigation. Yiming Zhu: Funding acquisition and Supervision. Shengjiang Chang: Funding acquisition and Supervision. Songlin Zhuang: Funding acquisition and Supervision.

Funding

This work was supported in part by National key research and development program of China (grant No. 2022YFA1404004), National Natural Science Foundation of China (grant No. 61988102, No. 62335012).

Availability of data and materials

The data generated and analyzed during this study are available from the corresponding author upon reasonable request.

Declarations

Ethics approval and consent to participate
All authors participate in this work and manuscript.

Consent for publication
All authors agree with the submission of this manuscript.

Competing interests
The authors declare no conflicts of interest.

Received: 22 February 2024 Revised: 18 March 2024 Accepted: 3 April 2024
Published online: 15 April 2024

References

1. Choi WJ, Yano K, Cha M, Colombari FM, Kim J-Y, Wang Y, Lee SH, Sun K, Kruger JM, de Moura AF, Kotov NA. Chiral phonons in microcrystals and nanofibrils of biomolecules. Nat Photonics. 2022;16(5):366–73. https://doi.org/10.1038/s41566-022-00969-1.
2. Lou J, Jiao YN, Yang RS, Huang YD, Xu X, Zhang L, Ma ZF, Yu Y, Peng WY, Yuan YF, Zhong Y, Li SY, Yan Y, Zhang FL, Liang JG, Du XH, Chang C, Qiu CW. Calibration-free, high-precision, and robust terahertz ultrafast metasurfaces for monitoring gastric cancers. Proceedings of the National Academy of Sciences of the United States of America. 2022;119(43). https://doi.org/10.1073/pnas.2209218119.
3. Peng Y, Shi C, Zhu Y, Gu M, Zhuang S. Terahertz spectroscopy in biomedical field: a review on signal-to-noise ratio improvement. PhotoniX. 2020;1(1). https://doi.org/10.1186/s43074-020-00011-z.
4. Zhang C, Yuan Y, Wu K, Wang Y, Zhu S, Shi J, Wang L, Li Q, Zuo X, Fan C, Chang C, Li J. Driving DNA origami assembly with a terahertz wave. Nano Lett. 2021;22(1):468–75. https://doi.org/10.1021/acs.nanolett.1c04369.
5. Ho L, Pepper M, Taday P. TERAHERTZ SPECTROSCOPY Signatures and fingerprints. Nat Photonics. 2008;2:541–3. https://doi.org/10.1038/nphoton.2008.174.
6. Niessen KA, Xu M, George DK, Chen MC, Ferré-D'Amaré AR, Snell EH, Cody V, Pace J, Schmidt M, Markelz AG. Protein and RNA dynamical fingerprinting. Nature Communications. 2019;10(1). https://doi.org/10.1038/s41467-019-08926-3.
7. Peng Y, Huang JL, Luo J, Yang ZF, Wang LP, Wu X, Zang XF, Yu C, Gu M, Hu Q, Zhang XC, Zhu YM, Zhuang SL. Three-step one-way model in terahertz biomedical detection. Photonix. 2021;2(1). https://doi.org/10.1186/s43074-021-00034-0.
8. Mayerhöfer TG, Popp J. Beer's Law - Why Absorbance Depends (Almost) Linearly on Concentration. ChemPhysChem. 2019;20(4):511–5. https://doi.org/10.1002/cphc.201801073.
9. Yang X, Zhao X, Yang K, Liu YP, Liu Y, Fu WL, Luo Y. Biomedical Applications of Terahertz Spectroscopy and Imaging. Trends Biotechnol. 2016;34(10):810–24. https://doi.org/10.1016/j.tibtech.2016.04.008.
10. Lee SH, Choe JH, Kim C, Bae S, Kim JS, Park QH, Seo M. Graphene assisted terahertz metamaterials for sensitive bio-sensing. Sensors and Actuators B-Chemical. 2020;310. https://doi.org/10.1016/j.snb.2020.127841.
11. Zhang XT, He LY, Gan X, Huang XC, Du YX, Zhai ZS, Li Z, Zheng YL, Chen XF, Cai YJ, Ao XY. Quasi-Bound States in the Continuum Enhanced Second-Harmonic Generation in Thin-Film Lithium Niobate. Laser & Photonics Reviews. 2022;16(9). https://doi.org/10.1002/lpor.202200031.
12 Kruk SS, Wang L, Sain B, Dong ZG, Yang J, Zentgraf T, Kivshar Y. Asymmetric parametric generation of images with nonlinear dielectric metasurfaces. Nat Photonics. 2022;16(8):561-+. https://doi.org/10.1038/s41566-022-01018-7.
13. Weber T, Kühner L, Sortino L, Ben Mhenni A, Wilson NP, Kühne J, Finley JJ, Maier SA, Tittl A. Intrinsic strong light-matter coupling with self-hybridized bound states in the continuum in van der Waals metasurfaces. Nat Materials. 2023;22(8):970-+. https://doi.org/10.1038/s41563-023-01580-7.
14. Zhou CB, Huang LJ, Jin R, Xu L, Li GH, Rahmani M, Chen XS, Lu W, Miroshnichenko AE. Bound States in the Continuum in Asymmetric Dielectric Metasurfaces. Laser & Photonics Reviews. 2023;17(3). https://doi.org/10.1002/lpor.202200564.
15. Zang X, Yao B, Chen L, Xie J, Guo X, Balakin AV, Shkurinov AP, Zhuang S. Metasurfaces for manipulating terahertz waves. Light: Advanced Manufacturing. 2021;2(2). https://doi.org/10.37188/lam.2021.010.
16. Zhu Y, Zang X, Chi H, Zhou Y, Zhu Y, Zhuang S. Metasurfaces designed by a bidirectional deep neural network and iterative algorithm for generating quantitative field distributions. Light: Advanced Manufacturing. 2023;4(2). https://doi.org/10.37188/lam.2023.009.
17. Bai ZY, Liu YS, Kong RR, Nie TX, Sun Y, Li HL, Sun T, Pandey CD, Wang YN, Zhang HY, Song QL, Liu GZ, Kraft M, Zhao WS, Wu XJ, Wen LG. Near-field Terahertz Sensing of HeLa Cells and Pseudomonas Based on Monolithic Integrated Metamaterials with a Spintronic Terahertz Emitter. ACS Appl Mater Interfaces. 2020;12(32):35895–902. https://doi.org/10.1021/acsami.0c08543.
18. Zhang J, Mu N, Liu LH, Xie JH, Feng H, Yao JQ, Chen TN, Zhu WR. Highly sensitive detection of malignant glioma cells using metamaterial-inspired THz biosensor based on electromagnetically induced transparency. Biosens Bioelectron. 2021;185:7. https://doi.org/10.1016/j.bios.2021.113241.
19. Jun SW, Ahn YH. Terahertz thermal curve analysis for label-free identification of pathogens. Nat Commun. 2022;13(1):8. https://doi.org/10.1038/s41467-022-31137-2.
20. Barth I, Conteduca D, Reardon C, Johnson S, Krauss TF. Common-path interferometric label-free protein sensing with resonant dielectric nanostructures. Light Sci Appl. 2020;9:96. https://doi.org/10.1038/s41377-020-0336-6.

21. Tang C, Yang J, Wang YD, Cheng J, Li XL, Chang C, Hu J, Lü JH. Integrating terahertz metamaterial and water nanodroplets for ultrasensitive detection of amyloid β aggregates in liquids. Sens Actuators B Chem. 2021;329:6. https://doi.org/10.1016/j.snb.2020.129113.
22. Wang RD, Xu L, Huang LJ, Zhang XB, Ruan H, Yang X, Lou J, Chang C, Du XH. Ultrasensitive Terahertz Biodetection Enabled by Quasi-BIC-Based Metasensors. Small. 2023;19(35):9. https://doi.org/10.1002/smll.202301165.
23. Shi WN, Fan F, Li SS, Zhang ZY, Liu HL, Wang XH, Chang SJ. Terahertz immunosensing assisted by functionalized Au NPs based on all-dielectric metasurface. Sens Actuators B Chem. 2022;362:10. https://doi.org/10.1016/j.snb.2022.131777.
24. Yang K, Li JN, de la Chapelle ML, Huang GR, Wang YX, Zhang JB, Xu DG, Yao JQ, Yang X, Fu WL. A terahertz metamaterial biosensor for sensitive detection of microRNAs based on gold-nanoparticles and strand displacement amplification. Biosens Bioelectron. 2021;175:7. https://doi.org/10.1016/j.bios.2020.112874.
25. Zhou RY, Wang C, Huang YX, Huang K, Wang YL, Xu WD, Xie LJ, Ying YB. Label-free terahertz microfluidic biosensor for sensitive DNA detection using graphene-metasurface hybrid structures. Biosens Bioelectron. 2021;188:8. https://doi.org/10.1016/j.bios.2021.113336.
26. Sengupta R, Khand H, Sarusi G. Terahertz Impedance Spectroscopy of Biological Nanoparticles by a Resonant Metamaterial Chip for Breathalyzer-Based COVID-19 Prompt Tests. Acs Applied Nano Materials. 2022;5(4):5803–12. https://doi.org/10.1021/acsanm.2c00954.
27. Zhang CB, Xue TJ, Zhang J, Li ZF, Liu LH, Xie JH, Yao JQ, Wang GM, Ye XD, Zhu WR. Terahertz meta-biosensor based on high-Q electrical resonance enhanced by the interference of toroidal dipole. Biosens Bioelectron. 2022;214:9. https://doi.org/10.1016/j.bios.2022.114493.
28. Wang YL, Dai BH, Ma C, Zhang Q, Huang K, Luo X, Liu XJ, Ying YB, Xie LJ. Cross-wavelength hierarchical metamaterials enabled for trans-scale molecules detection simultaneously. Adv Sci. 2022;9(13):8. https://doi.org/10.1002/advs.202105447.
29. Lee SH, Lee D, Choi MH, Son JH, Seo M. Highly sensitive and selective detection of steroid hormones using terahertz molecule-specific sensors. Anal Chem. 2019;91(10):6844–9. https://doi.org/10.1021/acs.analchem.9b01066.
30. Ma ZF, Jiao YA, Zhang CB, Lou J, Zhao PY, Zhang B, Wang YJ, Yu Y, Sun W, Yan Y, Yang XP, Sun L, Wang RD, Chang C, Li XR, Du XH. Identification and quantitative detection of two pathogenic bacteria based on a terahertz metasensor. Nanoscale. 2023;15(2):515–21. https://doi.org/10.1039/d2nr05038b.
31. Huang CC, Liang LJ, Chang PY, Yao HY, Yan X, Zhang YG, Xie YY. Terahertz Liquid Biosensor Based on A Graphene Metasurface for Ultrasensitive Detection with A Quasi-Bound State in the Continuum. Adv Mater. 2023:10. https://doi.org/10.1002/adma.202310493.
32. Banks PA, Kleist EM, Ruggiero MT. Investigating the function and design of molecular materials through terahertz vibrational spectroscopy. Nat Rev Chem. 2023;7(7):480–95. https://doi.org/10.1038/s41570-023-00487-w.
33. Schlauderer S, Lange C, Baierl S, Ebnet T, Schmid CP, Valovcin DC, Zvezdin AK, Kimel AV, Mikhaylovskiy RV, Huber R. Temporal and spectral fingerprints of ultrafast all-coherent spin switching. Nature. 2019;569(7756):383-+. https://doi.org/10.1038/s41586-019-1174-7.
34. Yan ZY, Zhu LG, Meng K, Huang WX, Shi QW. THz medical imaging: from in vitro to in vivo. Trends Biotechnol. 2022;40(7):816–30. https://doi.org/10.1016/j.tibtech.2021.12.002.
35 Tittl A, Leitis A, Liu MK, Yesilkoy F, Choi DY, Neshev DN, Kivshar YS, Altug H. Imaging-based molecular barcoding with pixelated dielectric metasurfaces. Science. 2018;360(6393):1105-+. https://doi.org/10.1126/science.aas9768.
36. Leitis A, Tittl A, Liu MK, Lee BH, Gu MB, Kivshar YS, Altug H. Angle-multiplexed all-dielectric metasurfaces for broadband molecular fingerprint retrieval. Sci Adv. 2019;5(5):8. https://doi.org/10.1126/sciadv.aaw2871.
37. Yesilkoy F, Arvelo ER, Jahani Y, Liu MK, Tittl A, Cevher V, Kivshar Y, Altug H. Ultrasensitive hyperspectral imaging and biodetection enabled by dielectric metasurfaces. Nat Photonics. 2019;13(6):390-+. https://doi.org/10.1038/s41566-019-0394-6.
38. Xie YN, Liu XY, Li FJ, Zhu JF, Feng NX. Ultra-wideband enhancement on mid-infrared fingerprint sensing for 2D materials and analytes of monolayers by a metagrating. Nanophotonics. 2020;9(9):2927–35. https://doi.org/10.1515/nanoph-2020-0180.
39. Chen XE, Zhang Y, Cai GX, Zhuo JL, Lai KZ, Ye LF. All-dielectric metasurfaces with high Q-factor Fano resonances enabling multi-scenario sensing. Nanophotonics. 2022;11(20):4537–49. https://doi.org/10.1515/nanoph-2022-0394.
40. Sun L, Xu L, Wang JY, Jiao YN, Ma ZH, Ma ZF, Chang C, Yang X, Wang RD. A pixelated frequency-agile metasurface for broadband terahertz molecular fingerprint sensing. Nanoscale. 2022;14(27):9681–5. https://doi.org/10.1039/d2nr01561g.
41. Zhu JF, Jiang S, Xie YN, Li FJ, Du LH, Meng K, Zhu LG, Zhou J. Enhancing terahertz molecular fingerprint detection by a dielectric metagrating. Opt Lett. 2020;45(8):2335–8. https://doi.org/10.1364/ol.389045.
42. Tan TC, Srivastava YK, Ako RT, Wang WH, Bhaskaran M, Sriram S, Al-Naib I, Plum E, Singh R. Active control of nanodielectric-induced THz quasi-BIC in flexible metasurfaces: a platform for modulation and sensing. Adv Mater. 2021;33(27):11. https://doi.org/10.1002/adma.202100836.
43. Hu YZ, Tong MY, Xu ZJ, Cheng XG, Jiang T. Bifunctional Spatiotemporal Metasurfaces for Incident Angle-Tunable and Ultrafast Optically Switchable Electromagnetically Induced Transparency. Small. 2021;17(21):10. https://doi.org/10.1002/smll.202006489.
44. Manjappa M, Pitchappa P, Singh N, Wang N, Zheludev NI, Lee C, Singh R. Reconfigurable MEMS Fano metasurfaces with multiple-input-output states for logic operations at terahertz frequencies. Nat Commun. 2018;9:10. https://doi.org/10.1038/s41467-018-06360-5.
45. Benea-Chelmus IC, Mason S, Meretska ML, Elder DL, Kazakov D, Shams-Ansari A, Dalton LR, Capasso F. Gigahertz free-space electro-optic modulators based on Mie resonances. Nat Commun. 2022;13(1):9. https://doi.org/10.1038/s41467-022-30451-z.
46. Yu P, Li JX, Liu N. Electrically tunable optical metasurfaces for dynamic polarization conversion. Nano Lett. 2021;21(15):6690–5. https://doi.org/10.1021/acs.nanolett.1c02318.

47. Fu XJ, Shi L, Yang J, Fu Y, Liu CX, Wu JW, Yang F, Bao L, Cui TJ. Flexible terahertz beam manipulations based on liquid-crystal-integrated programmable metasurfaces. ACS Appl Mater Interfaces. 2022;14(18):22287–94. https://doi.org/10.1021/acsami.2c02601.
48. Fu XJ, Yang F, Liu CX, Wu XJ, Cui TJ. Terahertz beam steering technologies: from phased arrays to field-programmable Metasurfaces. Advanced Optical Materials. 2020;8(3):22. https://doi.org/10.1002/adom.201900628.
49. Jiao YA, Lou J, Ma ZF, Cong LQ, Xu X, Zhang B, Li DC, Yu Y, Sun W, Yan Y, Hu SD, Liu BY, Huang YD, Sun L, Wang RD, Singh R, Fan YC, Chang C, Du XH. Photoactive terahertz metasurfaces for ultrafast switchable sensing of colorectal cells. Mater Horizons. 2022;9(12):10. https://doi.org/10.1039/d2mh00787h.
50. Tang PR, Li J, Du LH, Liu Q, Peng QX, Zhao JH, Zhu B, Li ZR, Zhu LG. Ultrasensitive specific terahertz sensor based on tunable plasmon induced transparency of a graphene micro-ribbon array structure. Opt Express. 2018;26(23):30655–66. https://doi.org/10.1364/oe.26.030655.
51 Li YY, Ferreyra P, Swan AK, Paiella R. Current-driven terahertz light emission from graphene plasmonic oscillations. Acs Photonics. 2019;6(10):2562-+. https://doi.org/10.1021/acsphotonics.9b01037.
52. Asgari M, Riccardi E, Balci O, De Fazio D, Shinde SM, Zhang JC, Mignuzzi S, Koppens FHL, Ferrari AC, Viti L, Vitiello MS. Chip-Scalable, Room-Temperature, Zero-Bias, Graphene-Based Terahertz Detectors with Nanosecond Response Time. ACS Nano. 2021;15(11):17966–76. https://doi.org/10.1021/acsnano.1c06432.
53. Rodrigo D, Limaj O, Janner D, Etezadi D, de Abajo FJG, Pruneri V, Altug H. Mid-infrared plasmonic biosensing with graphene. Science. 2015;349(6244):165–8. https://doi.org/10.1126/science.aab2051.
54. Koepfli SM, Baumann M, Koyaz Y, Gadola R, Güngör A, Keller K, Horst Y, Nashashibi S, Schwanninger R, Doderer M, Passerini E, Fedoryshyn Y, Leuthold J. Metamaterial graphene photodetector with bandwidth exceeding 500 gigahertz. Science. 2023;380(6650):1169–74. https://doi.org/10.1126/science.adg8017.
55. Wang ZF, Peng Y, Shi CJ, Wang LP, Chen XH, Wu WW, Wu X, Zhu YM, Zhang JC, Cheng GL, Zhuang SL. Qualitative and quantitative recognition of chiral drugs based on terahertz spectroscopy. Analyst. 2021;146(12):3888–98. https://doi.org/10.1039/d1an00500f.
56. Chen X, Fan WH, Song C. Multiple plasmonic resonance excitations on graphene metamaterials for ultrasensitive terahertz sensing. Carbon. 2018;133:416–22. https://doi.org/10.1016/j.carbon.2018.03.051.
57. Mou NL, Sun SL, Dong HX, Dong SH, He Q, Zhou L, Zhang L. Hybridization-induced broadband terahertz wave absorption with graphene metasurfaces. Opt Express. 2018;26(9):11728–36. https://doi.org/10.1364/oe.26.011728.
58. Geim AK, Novoselov KS. The rise of graphene. Nat Mater. 2007;6(3):183–91. https://doi.org/10.1038/nmat1849.
59. Yan HG, Low T, Guinea F, Xia FN, Avouris P. Tunable phonon-induced transparency in bilayer graphene nanoribbons. Nano Lett. 2014;14(8):4581–6. https://doi.org/10.1021/nl501628x.
60. Castilla S, Terrés B, Autore M, Viti L, Li J, Nikitin AY, Vangelidis I, Watanabe K, Taniguchi T, Lidorikis E, Vitiello MS, Hillenbrand R, Tielrooij KJ, Koppen FHL. Fast and Sensitive Terahertz Detection using an Antenna-Integrated Graphene pn Junction. Nano Lett. 2019;19(5):2765–73. https://doi.org/10.1021/acs.nanolett.8b04171.
61. Yan HG, Low T, Zhu WJ, Wu YQ, Freitag M, Li XS, Guinea F, Avouris P, Xia FN. Damping pathways of mid-infrared plasmons in graphene nanostructures. Nat Photonics. 2013;7(5):394–9. https://doi.org/10.1038/nphoton.2013.57.
62. Sensale-Rodriguez B, Yan RS, Kelly MM, Fang T, Tahy K, Hwang WS, Jena D, Liu L, Xing HG. Broadband graphene terahertz modulators enabled by intraband transitions. Nat Commun. 2012;3:7. https://doi.org/10.1038/ncomms1787.
63. Mao Q, Wen QY, Tian W, Wen TL, Chen Z, Yang QH, Zhang HW. High-speed and broadband terahertz wave modulators based on large-area graphene field-effect transistors. Opt Lett. 2014;39(19):5649–52. https://doi.org/10.1364/ol.39.005649.
64. Fang ZY, Thongrattanasiri S, Schlather A, Liu Z, Ma LL, Wang YM, Ajayan PM, Nordlander P, Halas NJ, de Abajo FJG. Gated Tunability and Hybridization of Localized Plasmons in Nanostructured Graphene. ACS Nano. 2013;7(3):2388–95. https://doi.org/10.1021/nn3055835.
65. Mousavi SH, Kholmanov I, Alici KB, Purtseladze D, Arju N, Tatar K, Fozdar DY, Suk JW, Hao YF, Khanikaev AB, Ruoff RS, Shvets G. Inductive Tuning of Fano-Resonant Metasurfaces Using Plasmonic Response of Graphene in the Mid-Infrared. Nano Lett. 2013;13(3):1111–7. https://doi.org/10.1021/nl304476b.
66. Wang L, An N, Gong S, Sheng X, Li YW, Yao BC, Yu C, He ZZ, Liu QB, Feng ZH, Otsuji T, Zhang YX. Ultrafast terahertz transparency boosting in graphene meta-cavities. Nanophotonics. 2022;11(21):4899–907. https://doi.org/10.1515/nanoph-2022-0511.
67. Kim J, Kuzyk MC, Han KW, Wang HL, Bahl G. Non-reciprocal Brillouin scattering induced transparency. Nat Phys. 2015;11(3):275–80. https://doi.org/10.1038/nphys3236.
68. Yang YM, Kravchenko II, Briggs DP, Valentine J. All-dielectric metasurface analogue of electromagnetically induced transparency. Nat Commun. 2014;5:7. https://doi.org/10.1038/ncomms6753.
69. Chiam SY, Singh R, Rockstuhl C, Lederer F, Zhang WL, Bettiol AA. Analogue of electromagnetically induced transparency in a terahertz metamaterial. Phys Rev B. 2009;80(15):4. https://doi.org/10.1103/PhysRevB.80.153103.
70. Ling YH, Huang LR, Hong W, Liu TJ, Luan J, Liu WB, Lai JJ, Li HP. Polarization-controlled dynamically switchable plasmon-induced transparency in plasmonic metamaterial. Nanoscale. 2018;10(41):19517–23. https://doi.org/10.1039/c8nr03564d.
71. Yahiaoui R, Burrow JA, Mekonen SM, Sarangan A, Mathews J, Agha I, Searles TA. Electromagnetically induced transparency control in terahertz metasurfaces based on bright-bright mode coupling. Phys Rev B. 2018;97(15):5. https://doi.org/10.1103/PhysRevB.97.155403.
72. Zhang Z, Gao J, Yang MS, Yan X, Lu YY, Wu L, Li JN, Wei DQ, Liu LH, Xie JH, Liang LJ, Yao JQ. Microfluidic integrated metamaterials for active terahertz photonics. Photonics Research. 2019;7(12):1400–6. https://doi.org/10.1364/prj.7.001400.
73. Yan X, Yang MS, Zhang Z, Liang LJ, Wei DQ, Wang M, Zhang MJ, Wang T, Liu LH, Xie JH, Yao JQ. The terahertz electromagnetically induced transparency-like metamaterials for sensitive biosensors in the detection of cancer cells. Biosens Bioelectron. 2019;126:485–92. https://doi.org/10.1016/j.bios.2018.11.014.

74. Afra D, Baron B, Bonadonna G, Curran WJ, Green SB, Hildebrand J, Scott CB, Shapiro W, Thomas D, Trojanowski T, Urtasun R, Walker MD, Burdett S, Parmar MKB, Souhami RL, Stenning SP, Stewart LA, Glioma Meta-analysis Trialists G. Chemotherapy in adult high-grade glioma: a systematic review and meta-analysis of individual patient data from 12 randomised trials. Lancet. 2002;359(9311):1011–8. https://doi.org/10.1016/S0140-6736(02)08091-1.
75. Peng Y, Shi CJ, Xu MQ, Kou TY, Wu X, Song B, Ma HY, Guo SW, Liu LZ, Zhu YM. Qualitative and Quantitative Identification of Components in Mixture by Terahertz Spectroscopy. Ieee Transact Terahertz Sci Technol. 2018;8(6):696–701. https://doi.org/10.1109/tthz.2018.2867816.
76. Liu XY, Chen W, Ma YJ, Xie YN, Zhou J, Zhu LG, Xu YD, Zhu JF. Enhancing THz fingerprint detection on the planar surface of an inverted dielectric metagrating. Photonics Research. 2022;10(12):2836–45. https://doi.org/10.1364/prj.472114.
77. Xie YN, Liu XY, Zhou J, Zhang HF, Lin JY, Chen W, Zhu LG, Meng K, Liu QH, Zhu JF. Enhancing Trace Terahertz Fingerprint Sensing by the Lossy Silicon Metagrating With a Gold Mirror. IEEE Trans Microw Theory Tech. 2023:10. https://doi.org/10.1109/tmtt.2023.3314094.
78. Xie YN, Ma YJ, Liu XY, Khan SA, Chen W, Zhu LG, Zhu JF, Liu QH. Dual-Degree-of-Freedom Multiplexed Metasensor Based on Quasi-BICs for Boosting Broadband Trace Isomer Detection by THz Molecular Fingerprint. IEEE J Sel Top Quantum Electron. 2023;29(5):10. https://doi.org/10.1109/jstqe.2023.3236981.
79. Xiao SY, Wang T, Liu TT, Yan XC, Li Z, Xu C. Active modulation of electromagnetically induced transparency analogue in terahertz hybrid metal-graphene metamaterials. Carbon. 2018;126:271–8. https://doi.org/10.1016/j.carbon.2017.10.035.
80. Chen MM, Xiao ZY, Lu XJ, Lv F, Zhou YJ. Simulation of dynamically tunable and switchable electromagnetically induced transparency analogue based on metal-graphene hybrid metamaterial. Carbon. 2020;159:273–82. https://doi.org/10.1016/j.carbon.2019.12.050.
81. Zeng BB, Huang ZQ, Singh A, Yao Y, Azad AK, Mohite AD, Taylor AJ, Smith DR, Chen HT. Hybrid graphene metasurfaces for high-speed mid-infrared light modulation and single-pixel imaging. Light-Sci Appl. 2018;7:8. https://doi.org/10.1038/s41377-018-0055-4.
82. Shi WQ, Gu JQ, Zhang XY, Xu Q, Han JG, Yang QL, Cong LQ, Zhang WL. Terahertz bound states in the continuum with incident angle robustness induced by a dual period metagrating. Photonics Res. 2022;10(3):810–9. https://doi.org/10.1364/prj.440741.
83 Liu HZ, Guo C, Vampa G, Zhang JYL, Sarmiento T, Xiao M, Bucksbaum PH, Vuckovic J, Fan SH, Reis DA. Enhanced high-harmonic generation from an all-dielectric metasurface. Nat Phys. 2018;14(10):1006-+. https://doi.org/10.1038/s41567-018-0233-6.
84. Kim TT, Kim HD, Zhao R, Oh SS, Ha T, Chung DS, Lee YH, Min B, Zhang S. Electrically Tunable Slow Light Using Graphene Metamaterials. ACS Photonics. 2018;5(5):1800–7. https://doi.org/10.1021/acsphotonics.7b01551.
85. Hu YZ, Tong MY, Hu SY, He WB, Cheng XA, Jiang T. Spatiotemporal Lineshape Tailoring in BIC-Mediated Reconfigurable Metamaterials. Adv Func Mater. 2022;32(34):11. https://doi.org/10.1002/adfm.202203680.

Publisher's Note